PHYSICAL SCIENCES

Charge-transfer dipole low-frequency vibronic excitation at single-molecular scale

Cancan Lou[1]†, Yurou Guan[2,3]†, Xingxia Cui[1]†, Yafei Li[1], Xieyu Zhou[2,3], Qing Yuan[1], Guangqiang Mei[1], Chengxiang Jiao[1], Kai Huang[1], Xuefeng Hou[1], Limin Cao[1], Wei Ji[2,3]*, Dino Novko[4], Hrvoje Petek[5]*, Min Feng[1,5,6]*

Scanning tunneling microscopy (STM) vibronic spectroscopy, which has provided submolecular insights into electron-vibration (vibronic) coupling, faces challenges when probing the pivotal low-frequency vibronic excitations. Because of eigenstate broadening on solid substrates, resolving low-frequency vibronic states demands strong decoupling. This work designs a type II band alignment in STM junction to achieve effective charge-transfer state decoupling. This strategy enables the successful identification of the lowest-frequency $H_g(\omega_1)$ (Raman-active H_g mode) vibronic excitation within single C_{60} molecules, which, despite being notably pronounced in electron transport of C_{60} single-molecule transistors, has remained hidden at submolecular level. Our results show that the observed $H_g(\omega_1)$ excitation is "anchored" to all molecules, irrespective of local geometry, challenging common understanding of structural definition of vibronic excitation governed by Franck-Condon principle. Density functional theory calculations reveal existence of molecule-substrate interfacial charge-transfer dipole, which, although overlooked previously, drives the dominant $H_g(\omega_1)$ excitation. This charge-transfer dipole is not specific but must be general at interfaces, influencing vibronic coupling in charge transport.

INTRODUCTION

Understanding electron-vibration, i.e., vibronic, coupling at the single-molecule level is of crucial importance for understanding of various physical phenomena in solids and their interfaces. This includes exploring intricate energy dissipation pathways (*1*–*6*) and correlated quantum states (*7*–*12*). Single-molecular transport measurements (*13*–*16*), accomplished by delicately creating a broken junction to assemble one molecule between the electrodes, have successfully revealed vibration-coupled currents within individual molecules. As the vibronic coupling strongly correlates with integral over the initial and final vibronic states (*17*–*19*), the analysis of the defining processes can face challenges because of the unresolved molecular adsorption configurations between the junctions.

To circumvent the orientational inhomogeneity, scanning tunneling microscopy (STM) vibronic spectroscopy is capable of detecting tunneling currents modulated by vibronic excitations with submolecular resolution (*5*, *20*–*29*). This contributes substantially to understanding of how molecular structural parameters affect vibronic excitations, such as the role of vibration itself (*5*, *30*), molecular electronic state's symmetries (*21*–*24*), and other factors (*25*–*28*, *31*). However, STM vibronic spectroscopy faces limitations when probing vibronic states associated with low-frequency vibrations, although they have been recognized critically relevant to charge transport in single molecules under nonequilibrium conditions (*13*, *14*, *27*, *32*, *33*). The situation is exemplified by C_{60}, which is one of the most extensively studied prototype molecules. C_{60} has eight Raman-active H_g modes (*34*), denoted as $H_g(\omega_1)$ to $H_g(\omega_8)$, with progressively increasing vibrational frequency. Despite evidence of multiple H_g modes of C_{60} being active in STM vibronic spectroscopy (*25*, *35*), the lowest-energy H_g mode, $H_g(\omega_1)$ with ~33-meV frequency, has remained undetected. This stands in a sharp contrast to C_{60} single-molecule transistor measurements (*13*), where $H_g(\omega_1)$ mode is detected as having an active role in electron transport.

The absence of the $H_g(\omega_1)$ signal in STM vibronic spectroscopy could be attributed to its energy broadening (Γ) on solid surfaces, defeating the eigenstate resolved vibronic spectroscopy on electronic substrates (*24*, *25*, *36*). To resolve individual vibronic states, Γ must be smaller than the associated vibrational quanta ($\hbar\omega$). Given that Γ is inversely proportional to the transient lifetime (τ) of vibronic states (indicated by $\Gamma\tau = \hbar$, where $\hbar$ is the reduced Planck constant) (*36*, *37*), previous STM studies introduced atomically thin insulating layers between the molecule and the metallic substrate to extend τ and thereby reduce Γ (*21*–*27*, *31*, *35*, *38*). The thickness of these isolating atomic spacers, however, must be constrained to enable successful tunneling, hindering continuous reduction of Γ by adding more layers of atomic spacers. This limitation makes it challenging to resolve the low-energy $\hbar\omega$ modes. In the case of C_{60}, the $H_g(\omega_2)$ mode of approximately 56 meV has been successfully detected in C_{60} adsorbed on thin oxide layers (*25*, *35*). The $H_g(\omega_1)$ mode, however, has eluded detection by such means.

Can Γ be further reduced in STM junctions to enable the detection of $H_g(\omega_1)$ vibronic state? In this study, we propose an effective strategy to decouple vibronic excitation from the substrate. By using a bulk semiconductor as the substrate, the molecular electronic states within the bulk bandgap are decoupled from the substrates, without introducing exogenous factors such as interface modification by introduction of insulating layers. Specifically, we achieve type II band alignment by supporting C_{60} molecules on the van der Waals (vdW) semiconductor SnSe(001) substrate (*39*–*41*), taking advantage of the lowest unoccupied molecular orbitals (LUMOs) of C_{60} extending below the conduction

[1]School of Physics and Technology and Key Laboratory of Artificial Micro- and Nano-Structures of Ministry of Education, Wuhan University, Wuhan 430072, China. [2]Beijing Key Laboratory of Optoelectronic Functional Materials & Micro-Nano Devices, School of Physics, Renmin University of China, Beijing 100872, China. [3]Key Laboratory of Quantum State Construction and Manipulation (Ministry of Education), Renmin University of China, Beijing 100872, China. [4]Centre for Advanced Laser Techniques, Institute of Physics, 10000 Zagreb, Croatia. [5]Department of Physics and Astronomy and IQ Initiative, University of Pittsburgh, Pittsburgh, PA 15260, USA. [6]Institute for Advanced Study, Wuhan University, Wuhan 430072, China.
*Corresponding author. Email: wji@ruc.edu.cn (W.J.); petek@pitt.edu (H.P.); fengmin@whu.edu.cn (M.F.)
†These authors contributed equally to this work.

band minimum (CBM) of SnSe, as is shown in Fig. 1. The p-doping of SnSe single crystal lowers its Fermi energy (E_F) below the valence band maximum (VBM), making it conductive to prevent charging of the STM junction.

STM measurements reveal that thermally evaporated C_{60} on SnSe(001) surfaces condenses into two types of islands, wherein C_{60} molecules exhibit three distinct STM contrasts. Combining with density functional theory (DFT) calculations, we determine the adsorption configurations of C_{60} molecules. The scanning tunneling spectroscopy differential current-voltage (dI/dV) spectra exhibit features induced by vibronic excitation in the LUMO resonances within the substrate's gap, with an energy-dependent Γ of 11 to 29 meV. The experimental data show that Γ decreases as vibronic states detune from the CBM, suggesting judicious design of the type II alignment to affect decoupling. Our finding promotes the application of type II band alignment to enhance decoupling in diverse electronic and energy harvesting systems.

Our experimental approach allows exposure of the previously concealed $H_g(\omega_1)$ vibronic excitation. Measurements of second differential d^2I/dV^2 spectra on different molecules resolve $H_g(\omega_1)$ vibronic peak progressions. In addition, we find that the $H_g(\omega_1)$ vibronic excitation is independent of the various molecular adsorption configurations and environmental conditions. This observation is contrary to common STM vibronic spectroscopy, which found that there is a sensitive relationship between the vibronic excitation and the local molecular configuration (*5*, *20*–*27*). Our DFT calculations unveil that a charge-transfer induced transient dipole plays a role in $H_g(\omega_1)$ vibrational excitation. This vibronic arrangement originates from interfacial charge redistribution upon electron tunneling, creating a transient interfacial dipole at C_{60}-SnSe interfaces. In C_{60} molecules, the charge density deformation accompanying specific $H_g(\omega_1)$ vibration exclusively causes a molecular charge fluctuation dipole to become nearly aligned with the interfacial dipole, enhancing its excitation over other H_g modes. These microscopic dipoles and their effects on vibronic excitations have been neglected in previous vibronic excitation studies (*20*–*27*).

RESULTS

Adsorption of C_{60} on SnSe(001)

C_{60} molecules evaporated onto SnSe form a compact film (Fig. 2A), featuring two alternating regions, for convenience, labeled region A and region B. These regions consistently alternate, with their extended boundaries (indicated by white dashed lines in Fig. 2A) aligned with the zigzag (*ZZ*) direction of the SnSe substrate. A closer look at region A, as presented in Fig. 2B, reveals that C_{60} molecules aggregate into a distinct superlattice, as delineated by the black dashed parallelogram in Fig. 2B. This supercell comprises five C_{60} molecules, displaying three distinct STM contrasts. The first category has an asymmetric two-lobed morphology (labeled as M_I), the second appears as a round protrusion (M_{II}), and the third takes shape of a symmetric two-lobed protrusion [$M_{III(1)}$]. In region B, a superlattice does not form, but C_{60} molecules appear with the same three STM contrasts distributed randomly (Fig. 2C). All correspond to M_I to M_{III} in region A, but M_{III} molecules in region B are oriented in a different direction, denoted as $M_{III(2)}$.

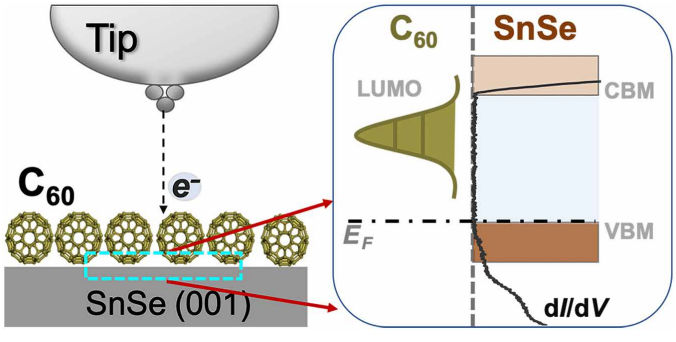

Fig. 1. Schematic description of the strategy to decouple molecular electronic states from substrates in an STM junction. The demonstration is accomplished by C_{60} adsorbing with its LUMO partially below the CBM of SnSe(001) surface. The E_F crosses VBM of SnSe.

Our DFT calculations reveal structural details of each configuration with input for the analysis from literature (*42*–*46*) (see text S1, table S1, and fig. S1 for more details). Configuration M_I is the most stable adsorption structure (Fig. 2D), with a C_{60} *h*:*h* ("*h*:*h*" denotes C═C bond of two side-by-side hexagons) bond adsorbed on a Sn-Sn vdW bridge site (Sn-vb-Sn). The *h*:*h* bond on the C_{60} top is parallel to the armchair (*AC*) direction of SnSe(001) (Fig. 2D). Configuration M_{II} is the second most stable, with a *h*:*p* ("*h*:*p*" denotes the C═C bond joining one pentagon and one hexagon) bond residing on top of the Se atom (Se-t) site and aligning with the *AC* direction (Fig. 2E). Configurations $M_{III(1)}$ and $M_{III(2)}$ correspond to *h*:*h* bonds adsorbed on Sn-Se vdW bridge sites (Sn-vb-Se), with a 45° inclination relative to the *AC* direction for $M_{III(1)}$ (Fig. 2F) and a 90° inclination for $M_{III(2)}$ (Fig. 2G), respectively.

In-gap LUMO resonances at C_{60}-SnSe(001) interfaces

Despite the presence of various adsorption configurations, the scanning tunneling spectroscopy dI/dV spectra demonstrate that all C_{60} on SnSe(001) surfaces exhibit semiconducting behavior characterized by well-resolved highest occupied molecular orbital (HOMO) and LUMO resonances (see fig. S2). Notably, the HOMO peaks consistently appear 1.7 to 1.8 eV below the VBM of SnSe, while the LUMO resonances partially overlap with the substrate's conduction band edge (fig. S2). This observation aligns with a type II band structure at the C_{60}-SnSe(001) interface, as depicted in Fig. 1. This type II band alignment is further illustrated in Fig. 3 (A to C), where dI/dV spectra are presented for three categories of C_{60} in regions A and B, as well as for a C_{60} located at an edge of a molecular island (M_E), representing typical molecules with diverse adsorption structures and varying local environments. Our detailed dI/dV measurements, as shown in fig. S3, exhibit that the dI/dV resonances do not shift under varying tip-C_{60} distances. This confirms the band alignment in the STM junction without being affected by molecule charging (*29*). This verification underscores the compatibility of the p-doped SnSe single-crystal substrate with effective electron tunneling in STM measurements.

In Fig. 3 (A to C), the LUMO resonances for all molecules exhibit a prominent three-peak feature with diminishing peak intensity. With the energy difference between the peaks being approximately 230 meV (refer to fig. S4 and text S2 for more details), as described in text S2, this feature could be attributed to the known Jahn-Teller dynamical resonances of C_{60} (*47*–*52*).

Expanding the dI/dV LUMO resonances below the CBM of SnSe reveals additional features that depend on the adsorption character. As shown in Fig. 3 (D to F), the onset energies of LUMO of C_{60} relative to

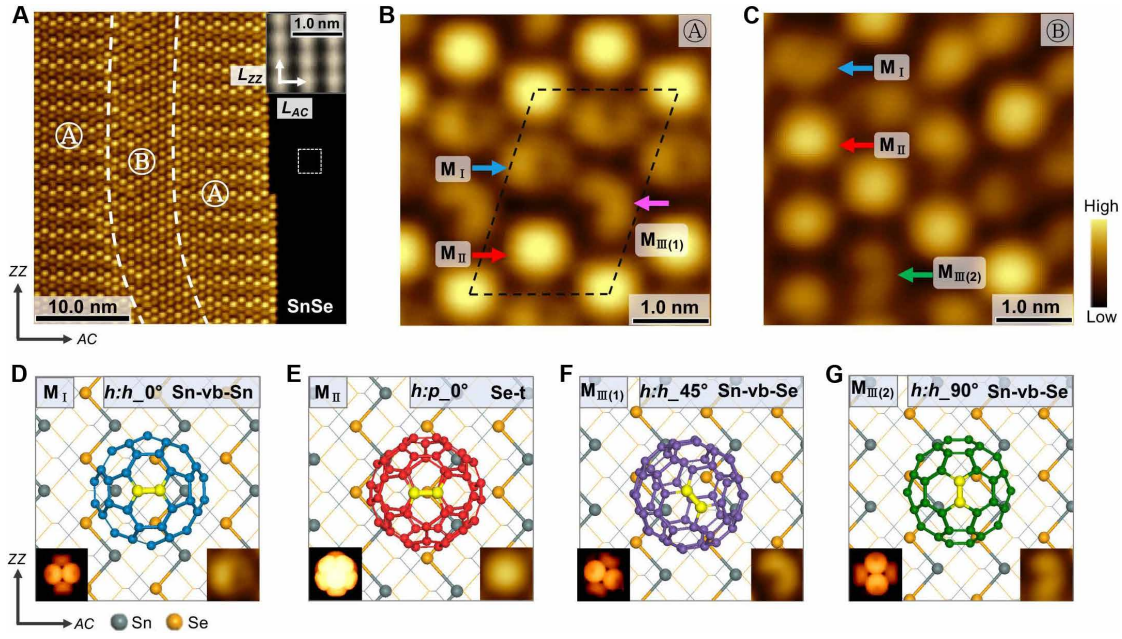

Fig. 2. Adsorption structures of C_{60} on SnSe(001) surface. (**A**) STM topographic image (V_b = 2.0 V, I_t = 5 pA) of a typical C_{60} monolayer island. Regions A and B within C_{60} island are marked. The top-right inset shows the resolved Sn atoms (V_b = −1.0 V, I_t = 20 pA) on SnSe substrate near the island, confirming the alignment of the boundaries between regions A and B. The measured lattice constants of the rectangular unit cell of SnSe is L_{ZZ} = 4.1 ± 0.2 Å and L_{AC} = 4.4 ± 0.2 Å in the *ZZ* and *AC* directions, respectively. (**B**) A close-up STM image (V_b = 1.3 V, I_t = 10 pA) of C_{60} in region A showing the parallelogram unit cell of the superlattice. The supercell is composed of three categories of C_{60} molecules with distinct STM contrasts marked by M_I, M_{II}, and $M_{III(1)}$. (**C**) A close-up STM image (V_b = 1.3 V, I_t = 10 pA) of region B where C_{60} with the same three categories of typical STM contrasts are denoted as M_I, M_{II}, and $M_{III(2)}$. (**D** to **G**) DFT calculated adsorption configurations for M_I, M_{II}, $M_{III(1)}$, and $M_{III(2)}$. The C═C bond for adsorption is highlighted by yellow color. The theoretical STM contrasts (bottom-left) and the experimental images (bottom-right) of these C_{60} molecules are displayed in the insets in (D) to (G), respectively.

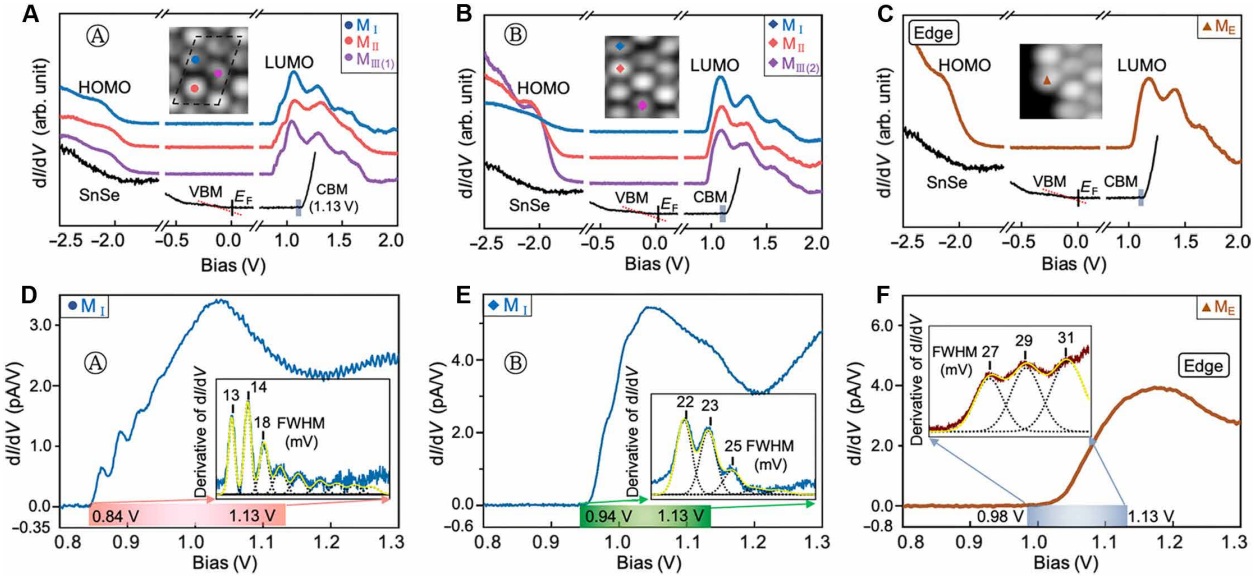

Fig. 3. d*I*/d*V* spectra of C_{60} molecules and in gap LUMO resonances. (**A** to **C**) d*I*/d*V* (V_b = 1.3 V, I_t = 150 pA) spectra from M_I, M_{II}, and $M_{III(1)}$ in region A; M_I, M_{II}, and $M_{III(2)}$ in region B; and from M_E at the island edge. The measurement locations are marked by the colored markers in (A) to (C). d*I*/d*V* spectrum of bare SnSe substrate is also provided to show the energy sites of VBM and CBM. Arb. unit, arbitrary unit. (**D** to **F**) Expanded LUMO resonance of M_I molecule in regions A, B, and M_E. The detuning of the C_{60} LUMO onset from the CBM of SnSe substrate is marked with the pink, green, and blue shadings. The insets show the numerical derivatives of the d*I*/d*V* spectra within the energy ranges defined by the colored shadings. The black dotted curves illustrate the Gaussian fittings of the peaks, and the yellow curves are their sums. The numbers give the extracted FWHM of the fitted peaks. All other markers in (D) to (F) are the same as those in (A) to (C).

CBM vary for different regions, namely, ~0.84 eV in region A, ~0.94 eV in region B, and ~0.98 eV at island edges (see text S3 for more details). This defines the energy difference between the onset of LUMO and the CBM of substrate for different molecules that is highlighted by the colored panels in Fig. 3. For C_{60} in region A, exemplified by M_I (M_{II} and M_{III} molecules show similar results) in Fig. 3D, pronounced saw-like peak shoulders emerge near the LUMO onset. These saw-like features diminish in intensity (Fig. 3E) for C_{60} in region B, where the LUMO onset is closer to CBM compared to that for C_{60} in region A. For M_E, located close to CBM (Fig. 3F), these features are barely observable. Regarding the HOMO, which consistently lies deeper than the VBM of SnSe (fig. S2), these resonances cannot be resolved.

The saw-like feature in the dI/dV spectra has been identified as conductance modulation by vibronic excitation (*24*–*26*). The fact that this feature exclusively appears in the energy window where molecular states overlap with the substrate's bandgap suggests that the observed molecular vibronic states are considerably decoupled from those of the substrate. This decoupling persists as long as the molecular states are energetically constrained from overlapping with propagating states of the substrate conduction band. That is, the below gap molecular LUMO features are surface states with wave functions that evanescently penetrate substrates, whereas molecular states above the bandgap are resonances with wave functions that hybridize with the propagating states of the substrate. This transition is well known for surface image potential states (*53*–*55*) and resonances. The molecular wave function penetration into the substrate opens new decay channels that are sensitive to its extent. This is observed by numerically differentiating the dI/dV and analyzing the resulting derivative peaks (shown in the insets in Fig. 3, D to F), which correspond to vibronic peaks that represent the abrupt conductance changes due to vibronic excitation. By performing Gaussian fitting on these derivative peaks to estimate the full width at half maximum (FWHM) as Γ, we observe an increase in FWHM values (insets in Fig. 3, D to F) as the energy difference between the C_{60} LUMO onset and the CBM of SnSe decreases. Specifically, the FWHM of the first vibronic peak is ~13 mV for M_I in region A (Fig. 3D), ~22 mV for M_I in region B (Fig. 3E), and ~27 for M_E (Fig. 3F). Moreover, Γ increases within the series of vibronic peaks as the vibronic excitation approaches the CBM of the substrate. This is demonstrated by the FWHM of the first three pronounced peaks, which increases from ~13 to ~18 mV for M_I in region A (Fig. 3D), from ~22 to ~25 mV for M_I in region B (Fig. 3E), and from ~27 to ~31 mV for M_E (Fig. 3F). This trend is further corroborated in subsequent discussions where the second harmonic of the ac tunneling current, d^2I/dV^2, recorded simultaneously with the dI/dV spectra, captures the vibronic excitation signals with higher contrast.

$H_g(\omega_1)$ vibrational excitation in C_{60}

Recording d^2I/dV^2 reveals clear resolution of the Hg(ω_1) vibronic excitations (see fig. S5 for the simultaneously recorded dI/dV and d^2I/dV^2 spectra). Our measurements indicate that the d^2I/dV^2 spectra are repeatable under varying measurement parameters (fig. S6). In Fig. 4 (B to D), we present typical d^2I/dV^2 for M_I, M_{II}, and $M_{III(1)}$ molecules in region A. All spectra consist of a series of periodically spaced peaks. Similar phenomena are observed for M_I, M_{II}, and $M_{III(2)}$ C_{60} in region B (Fig. 4, F to H). We note that detailed measurements within single molecules reveal location-dependent shapes of the spectra, which, however, do not influence the following discussions and will be comprehensively described elsewhere. Following established protocols for analyzing vibronic states, each d^2I/dV^2 spectrum is fitted to a series of Gaussian peaks (*21*, *56*) but includes state-dependent

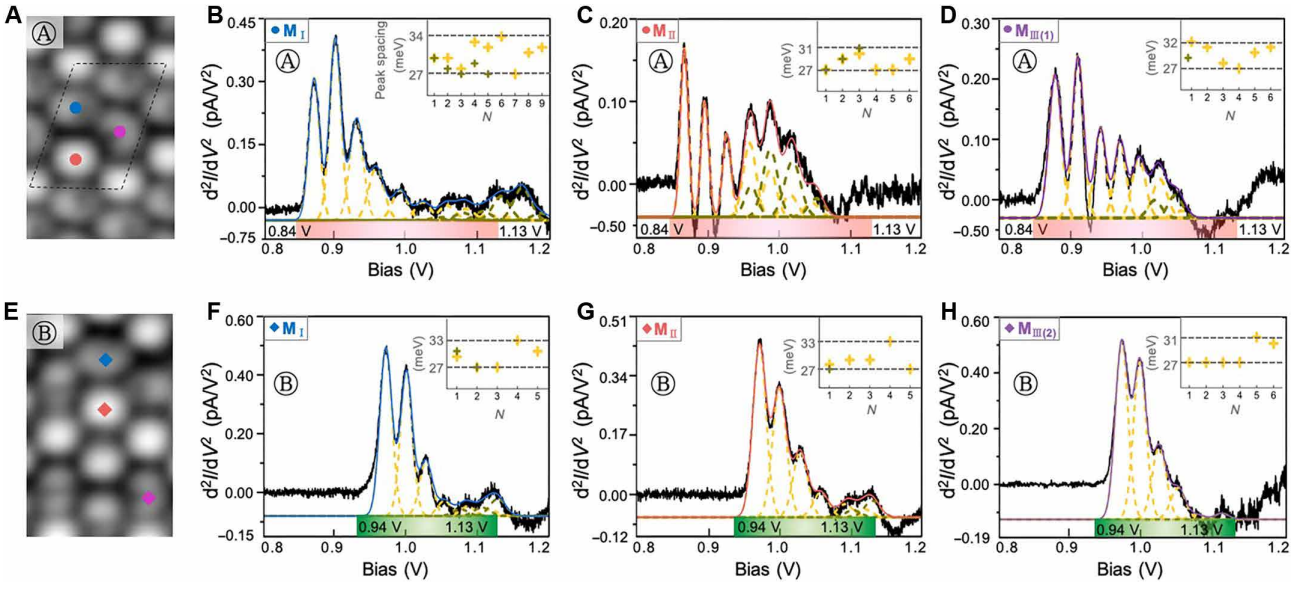

Fig. 4. $H_g(\omega_1)$ excitation in d^2I/dV^2 spectra of C_{60} molecules. (**A**) STM image of M_I, M_{II}, and $M_{III(1)}$ in region A. The colored dots mark the measurement sites of d^2I/dV^2 spectra. (**B** to **D**) d^2I/dV^2 (V_b = 1.3 V, I_t = 500 pA) spectra for M_I, M_{II}, and $M_{III(1)}$ in region A, respectively. The pink shading marks the energy window between the LUMO onset and CBM of substrate. The black color highlights the original spectra. The yellow and green dashed curves are the fitted two progressions, respectively. Their summation is represented by the blue, red, and purple curves in (B) to (D), respectively. The insets in (B) to (D) show the energy spacing between adjacent peaks with "*N*" marking the series of the energy spacing in the spectra. (**E**) STM image of M_I, M_{II}, and $M_{III(1)}$ in region B. The colored rhombus marks the measurement sites of d^2I/dV^2 spectra. (**F** to **H**) d^2I/dV^2 (V_b = 1.3 V, I_t = 500 pA) spectra for M_I, M_{II}, and $M_{III(1)}$ in region B, respectively. The green shading marks the energy window between the LUMO onset and CBM of substrate. All other presentations and markers in (B) to (D) are the same as those in (F) to (H).

FWHM, which gradually increases as discussed earlier. In Fig. 4, the summation of the fitting results, represented by the blue, red, and purple curves for C_{60} with different adsorption configurations, reproduces well the experimental data (represented by the black curves). In fig. S7, we present the relation between the fitted FWHM of the d^2I/dV^2 peaks with their energy differences relative to the CBM of the substrate. The data demonstrate that as the vibronic states drop below the CBM, their FWHM decreases. This shows that detuning below the CBM decreases inelastic coupling to the substrate that decreases Γ. Therefore, our strategy reveals the possibility of controlling the coupling by design of the type II alignment of molecule-semiconductor interface, a methodology that is broadly applicable.

The Gaussian fitting of d^2I/dV^2 spectra show that they can be decomposed into at least two progressions of equally spaced peaks (details provided in text S4 and fig. S7) (*19*, *57*). The two progressions are represented by the yellow and green dashed curves in Fig. 4 (B to D) and in Fig. 4 (F to H). Plotting the energy spacings between adjacent peaks in every sequence (insets in Fig. 4, B to D and F to H) obtains a consistent value of 30 ± 3 mV for the all the fitted data. The same spacing was obtained in d^2I/dV^2 spectrum for M_E (inset in Fig. 3F).

The equidistant peaks in the d^2I/dV^2 spectra are recognized as the excitation of an integer number of vibrational quanta of a transiently charged molecular state by tunneling electrons, known as a vibronic progression. Tunneling electrons excite a vibronic progression, with the energy spacing between the peaks corresponding to energy of the vibrational quanta (*21*, *24*–*26*). For C_{60} grown on a thin aluminum oxide film on NiAl(110) layers, vibronic progressions with an energy spacing of 56 ± 2, 94 ± 3, 138 ± 2, 150 ± 2, and 65 ± 4 meV have been attributed, respectively, to vibronic excitation of $H_g(\omega_2)$, $H_g(\omega_4)$, $H_g(\omega_5)$, $H_g(\omega_6)$, and $A_g(\omega_1)$ vibronic states of the transiently charged C_{60}^- anion (*25*, *35*). In our measurements, the observed series of peaks with a spacing of 30 ± 3 meV align with the energy quantum of $H_g(\omega_1)$ vibration of a free C_{60} (*34*, *58*). Given that C_{60} is adsorbed on SnSe surfaces with four types of adsorption configurations in the experiments, we calculate the energy quantum of the $H_g(\omega_1)$ mode for C_{60} adsorbed on SnSe(001) surface (see table S2). Upon adsorption on SnSe, the fivefold-degenerate $H_g(\omega_1)$ modes (*34*) retain their degeneracy, with the energy quantum consistently close to approximately 32 meV for all the studied adsorption configurations (table S2). Therefore, we attribute the observed progressions to the excitation of multiple quanta of the $H_g(\omega_1)$ mode of C_{60}.

To the best of our knowledge, these results represent the first instance of clearly resolving the C_{60} $H_g(\omega_1)$ vibronic excitation with single-molecular resolution. Our approach of taking advantage of the bulk gap of a semiconductor to decouple the vibronic states from the substrate is similar to the strategy of suspending individual single-walled carbon nanotube above a trench for measuring vibration-modulated current (*59*–*61*). In our study, the appropriate type II band alignment decouples adsorbate-substrate interaction accomplishing the same goal.

The charge-transfer dipole $H_g(\omega_1)$ vibronic excitation

Figure 4 reveals another aspect: The spectra are consistently dominated by the $H_g(\omega_1)$ progressions for all measured molecules, regardless of their adsorption configuration and local environment. This is in contrast to what is commonly observed for vibronic excitations (*21*–*26*, *35*).

Vibronic excitations are a consequence of nuclear motion to new geometry in response to a sudden electronic excitation (*21*–*26*, *62*–*66*). Intuitively, one might expect a molecule to deform depending on the specific molecular adsorption geometry and the unique local environment (*21*–*25*). This notion is asserted in the Franck-Condon (FC) principle of electronic excitation, where the excitation probability of a vibrational mode and its harmonics is determined by the vibronic overlap integral of the initial and final states (*17*–*19*). The FC principle finds extensive experimental support in the gas phase, where specific vibronic progressions communicate the nuclear structure rearrangement in electronic excitations (*5*, *30*, *67*). The same can happen for molecules adsorbed on surfaces, where the excited vibronic modes communicate changes in the structure of molecular electronic states that are simultaneously affected by the adsorption geometry (*21*–*24*), the neighboring molecules (*25*, *35*), the underlying substrate (*24*, *27*), the symmetry of the electronic states of last tip atom (*23*, *68*), and vibrationally mediated perturbations of the molecular electronic wave functions (*22*, *23*). In the case of C_{60}, for instance, $H_g(\omega_2)$, $H_g(\omega_5)$, and $H_g(\omega_6)$ modes were detected for molecules with orientations of the *h*, *h*:*h*, and *h*:*p* parallel to substrate surfaces (*25*). Our discovery of the dominant $H_g(\omega_1)$ vibronic signal prompts further inquiry into its origin.

Contrary to conventional expectations, our findings align with previous observations of inelastic carrier scattering in single C_{60} transistors (*13*), where $H_g(\omega_1)$ vibronic signals persist irrespective of possible variations in C_{60} adsorption structures across different devices. This exceptional result motivates effort exploring its excitation mechanism. Given that C_{60} assumes a transient anionic state during electron tunneling, we used DFT to compute the electronic structures of neutral C_{60} and negatively charged C_{60}^- adsorbed on the SnSe substrate (fig. S8). Upon adsorption onto the SnSe surface, the originally threefold-degenerate LUMO states of free C_{60} lose their degeneracy, resulting in energetically separated LUMO states denoted as LUMO-a, LUMO-b, and LUMO-c states. For neutral C_{60}, representing the M_I, M_{II}, $M_{III(1)}$, and $M_{III(2)}$ adsorption configurations, all three LUMO orbitals energetically sit within the bandgap of the SnSe substrate, without undergoing any electronic hybridization with SnSe substrate (fig. S8, B, E, H, and K). In the case of C_{60}^-, upon an electron injecting into the C_{60} molecule, the LUMO orbitals of C_{60} and the unoccupied bands of SnSe both shift downward to the E_F (fig. S8, C, F, I, and L). Although there is a partial energy overlap of the LUMO-b and LUMO-c orbitals with the CBM of SnSe near the *Y* points, LUMO-a, the lowest in energy among all three LUMO orbitals, remains below the CBM of SnSe. This finding is consistent with the experimental observations of the low-energy tail of the LUMO resonances aligned below the CBM of SnSe.

We then explore the electron redistribution at the C_{60}-SnSe interface upon injecting of an external electron by computing the differential charge densities (DCDs) between of a C_{60}^- anion and a neutral C_{60} molecules adsorbed on SnSe ($\rho_{DCD} = \rho_{anion} - \rho_{neutral}$). Here, ρ stands for the electron density. Figure 5A illustrates the DCD for the M_I configuration, where an electron is introduced to the neutral C_{60} molecule in its equilibrium geometry. This model represents the initial state of the system after adding an extra electron. In Fig. 5A, the black curve depicts the calculated charge variation perpendicular to the SnSe surface; it reveals a distinct dipole forming at C_{60}-SnSe interfaces, indicated by the thick gray arrow pointing from C_{60} to the surface. Analysis of the DCD for alternative C_{60} adsorption configurations, such as M_{II}, $M_{III(1)}$, and $M_{III(2)}$ (fig. S9), reveals analogous

interfacial dipoles. The independence of the formed dipole from specific structures confirms that the surface-normal dipole is robust at the C_{60}-SnSe interface in the initial after adding an electron. The geometry would then dynamically respond to the excess electron, forming a dipole field modulation at the C_{60}^--SnSe interface. We further verified whether the interfacial dipole persists at the final-state extreme, the opposite extreme compared to the initial state depicted in Fig. 5A, where the atomic structures were fully relaxed to respond the excess electron. According to the corresponding DCDs (fig. S10), a notable interfacial dipole persists, establishing the general existence of a perpendicular dipole at the C_{60}-SnSe interfaces upon doping with an excess electron.

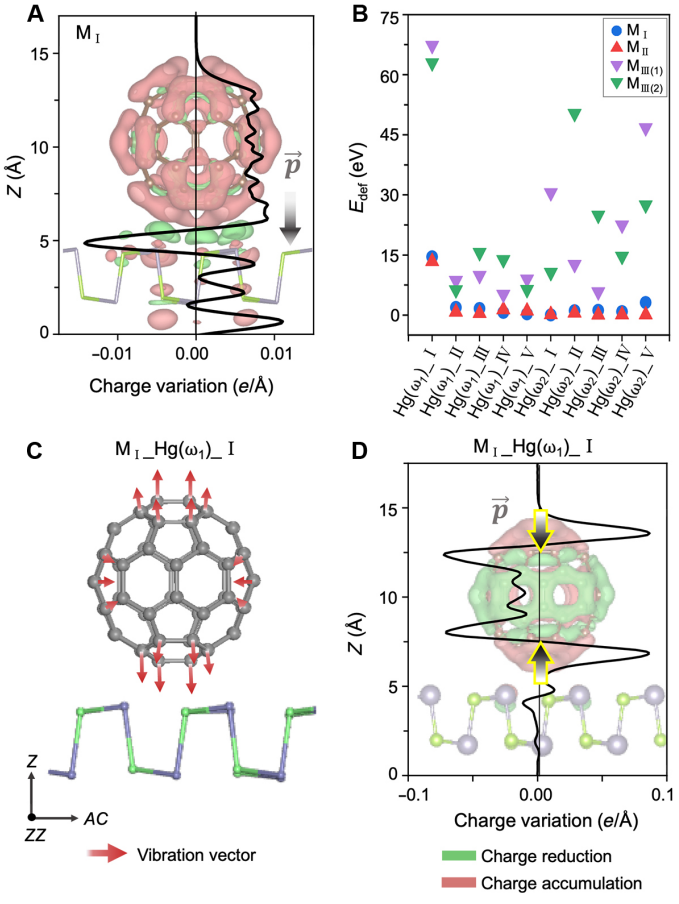

Fig. 5. The C_{60}-SnSe interfacial dipole and the Hg(ω_1)_I vibration-induced dipole. (**A**) Side view of the DCD between C_{60}^- and C_{60} on SnSe surface with M_I configuration. $\rho_{DCD} = \rho_{anion} - \rho_{neutral}$ (ρ stands for the electron density). The isosurface value is 0.0004 *e*/bohr^3. Red and green contours indicate charge accumulation and reduction, respectively. The black curve represents the integral charge variation in the direction perpendicular to SnSe surface. The gray arrow with $\vec{p}$ marks the polarity of the interfacial dipole. (**B**) Deformation energies (E_{def}) for the fivefold-degenerate Hg(ω_1) and Hg(ω_2) modes of C_{60} adsorbed on SnSe in configurations M_I, M_{II}, $M_{III(1)}$, and $M_{III(2)}$. Each E_{def} energy presented in the panel is the square root of the multiplication of the E_{def} values for the calculated neutral C_{60} and negatively charged C_{60}^-. (**C**) Side view of the vibrational vector of the Hg(ω_1)_I mode for C_{60} adsorbed on SnSe surface with M_I configuration. (**D**) Side views of the DCD representing $H_g(\omega_1)$_I vibration-induced dipole for a C_{60}^-. $\rho_{DCD} = \rho_{total\_equilibrium} - \rho_{total\_Hg(\omega_1\_I)}$ (ρ stands for the total electron density). The yellow edged gray arrow with $\vec{p}$ marks the polarity of the vibration-induced dipole.

We expanded our investigation to examine excess electron–triggered vibronic coupling in C_{60}-SnSe. Direct calculation of the vibronic coupling strength for such a large interface poses a huge challenge to the state-of-the-art DFT. As an alternative, we used the deformation potential (V_{def}) method, a practical approach for estimating vibronic coupling strength (see Materials and Methods for details) (*69*). The following discussion focuses on the $H_g(\omega_1)$ and $H_g(\omega_2)$ modes of C_{60}. The $H_g(\omega_2)$ mode represents higher-energy Raman-active H_g modes [from $H_g(\omega_2)$ to $H_g(\omega_8)$] characterized by shear atomic motions, which is absent in $H_g(\omega_1)$.

Considering the fivefold degeneracy of either $H_g(\omega_1)$ or $H_g(\omega_2)$ mode (*34*) [denoted as $H_g(\omega_1)$_I to $H_g(\omega_1)$_V and $H_g(\omega_2)$_I to $H_g(\omega_2)$_V in our subsequent discussion], the C_{60} adsorption configurations, and the transient charge state in tunneling process, we plotted 80 V_{def} curves in fig. S12. Figure 5B presents the deformation energy (E_{def}; integration of V_{def}; see Materials and Methods for details) of each mode in each adsorption configuration, providing a more comparable measure of V_{def}. The data show that the E_{def} value for the Hg(ω_1)_I mode is consistently the highest compared to other modes in every adsorption configuration. Specifically, the E_{def} of $H_g(\omega_1)$_I (~15 eV) is about an order of magnitude larger than those of other modes (close ~1) in the M_I (blue dots) and M_{II} configurations (red triangles). The predominant E_{def} value of $H_g(\omega_1)$_I among all considered cases indicates strong vibronic coupling of this mode for C_{60} on the SnSe surface. These quantitative results are consistent with the experimental observation of dominant $H_g(\omega_1)$ vibronic excitations for all measured molecules, regardless of adsorption configuration and local environment.

To explore the origin of the notable V_{def} of $H_g(\omega_1)$_I, we examined vibrational displacements, a portion for deriving V_{def}, in each $H_g(\omega_1)$ and $H_g(\omega_2)$ mode. We depicted the vibrational displacements for the $H_g(\omega_1)$_I mode in the M_I configuration in Fig. 5C, which exhibits a "breathing" motion of C atoms with vibrational vectors nearly perpendicular or parallel to the surface. Similar breathing displacements were presented for the $H_g(\omega_1)$_II to $H_g(\omega_1)$_V modes in fig. S11; however, their displacement vectors are appreciably off the normal axis of the SnSe surface. For the $H_g(\omega_2)$ modes, as shown in fig. S11, the vibrational displacements are more complex because of the presence of shear motions. Therefore, $H_g(\omega_1)$_I stands out by exhibiting an atomic displacement field normal to the surface.

The electron density variation, another determinant of V_{def}, is reflected by a DCD plot between the equilibrium and deformed atomic structures. In the latter, maximum vibrational displacements were added to the equilibrium structure. Figure 5D depicts the DCD for $H_g(\omega_1)$_I at the C_{60}^--SnSe interface in the M_I configuration, indicating that electron density variations mostly follow the vibrational displacement field of $H_g(\omega_1)$_I as shown in Fig. 5C. The vibration introduces charge accumulations on the top and bottom of the C_{60}^- and charge reduction in the middle region, forming a pair of electrical dipoles. This pair of dipoles exhibit the largest integrated charge variation perpendicular to the surface among the 10 $H_g(\omega_1)$ and $H_g(\omega_2)$ modes (refer to fig. S13), well aligned with the C_{60}-SnSe interfacial dipole identified in Fig. 5A. We infer that the coupling of these two dipoles substantially contributes to the largest V_{def} values for $H_g(\omega_1)$_I. The pronounced dipoles induced by vibration in the $H_g(\omega_1)$_I mode are also observable in M_{II}, $M_{III(1)}$, and $M_{III(2)}$ configurations (fig. S14). By comparing the $H_g(\omega_1)$_I-induced DCD (fig. S14) and the interfacial charge redistribution (fig. S9) for the four adsorption configurations, we conclude

that the dipole-dipole interaction enhances V_{def} for these adsorption configurations.

Through additional DFT calculations, we further establish a connection between the $H_g(\omega_1)$_I-induced electronic density polarity and the orbital-resolved electron probability density. Specifically, we confirm that, for C_{60} with each adsorption configuration, $H_g(\omega_1)$_I uniquely generates the charge polarity by coupling with the lowest-energy LUMO-a orbital, as opposed to the higher-energy LUMO-b and LUMO-c orbitals (details in fig. S15). These universal properties are consistent with the observed prevalence of $H_g(\omega_1)$ vibronic excitations with LUMO-a states in C_{60} across all observed adsorption configurations. Considering the possibility of similar interfacial dipole and vibrational dipole at C_{60}-electrode interfaces in single C_{60} transistors, our discovery provides insight into the consistent appearance of $H_g(\omega_1)$ vibronic signals in multiple devices where C_{60} adsorption configurations may vary (*13*, *14*).

DISCUSSION

In this study, we demonstrate the efficacy of using general type II band alignment in STM-molecule-substrate junctions for decoupling vibronic states of a molecule. This junction facilitates the emergence of the long-hidden C_{60} $H_g(\omega_1)$ vibronic excitation, with resolution of molecular adsorption structure. Our experimental results reveal that the decoupling of C_{60}^- LUMO strengthens as its energy is lowered into the gap of the substrate. This opens the potential to resolve low-frequency vibronic excitations with submolecular resolution for other prototype molecules, nanostructures, or ultrathin films on surfaces by judicious selection of semiconducting substrates for the properties of adsorbates. The proposed molecule-substrate pairs include, but are not limited to, molecules exhibiting electron tunneling–coupled vibronic excitations, such as CuPc (*24*) or NPc (*21*), where several predicted low-energy Raman-active vibronic states still wait experimental verification (*70*, *71*), on p-doped semiconductors such as SnSe(001) (*39*, *40*); or molecules characterizing hole tunneling–coupled vibronic excitations, such as phthalocyanine (H_2Pc) or 2,5-bis(3-dodecylthiophen-2-yl)thieno[3,2-b]-thiophene (*22*, *30*), where different vibronic excitation phenomena have been found compared to their electron counterparts, on n-doped semiconductors such as $SnSe_2$(001) (*72*).

The single-molecular resolution imaging of the $H_g(\omega_1)$ vibronic excitation unveils a crucial factor influencing vibronic coupling for molecular overlayers: the transient formation of an interfacial dipole upon electron tunneling into molecules. Fundamentally, the interfacial dipole arises from the universal screening effect (*73*): In response to charge injection into a molecular overlayer, molecules and substrates collectively respond to minimize free energy (dielectric screening), forming transient dipoles at molecule-substrate interfaces. Our discovery of the preferred and dominant $H_g(\omega_1)$ vibronic excitation for C_{60} on SnSe exemplifies this phenomenon, where the specific $H_g(\omega_1)$ mode, characterized by vibrational polarity aligned with the interfacial dipole, is enhanced. The substrate-involved charge-transfer dipole vibronic excitation has been previously overlooked in STM vibronic studies and discussions related to the fundamental FC principle governing vibronic excitation. Given the ubiquity of molecule-semiconductor interfaces, our strategy offers guidance for exploring similar effects in other systems, encompassing organic (opto) electronics, photovoltaic cells, two-dimensional vdW heterojunction-based devices, and beyond.

MATERIALS AND METHODS

Sample preparation

The high-quality SnSe single crystals used in the experiments are home-grown using the temperature gradient growth method from high-purity (99.9999%) Sn and Se granules. First, Sn and Se granules with the stoichiometry of SnSe and a total weight of 30 g are loaded into a quartz ampoule with an inner diameter of 11 mm. Then, the ampoule is evacuated to $<5 \times 10^{-5}$ torr and sealed. The primary ampoule is inserted into another quartz tube, which is evacuated and sealed to protect the sample and ampoule. The double-sealed quartz tube is loaded into a tubular furnace at a 15° angle from the horizontal plane. The sample in the furnace is slowly heated to 980°C over 30 hours, then is kept at this temperature for another 48 hours, and then lastly cools from 980° to 500°C at a precisely controlled rate of 1°C/hour. After cooling the furnace to room temperature (RT), the synthesized SnSe single crystals are taken out from the quartz ampoule to be used for the experiments.

Before the C_{60} growth and STM experiments, the SnSe crystals are cleaved in situ in a preparation chamber under ultrahigh vacuum (UHV) at RT. C_{60} molecules (99.99% purity; Sigma-Aldrich) are sublimated from a resistively heated evaporator onto a freshly prepared SnSe(001) surface. The SnSe substrates are kept at RT during the evaporation. The prepared sample is immediately transferred under UHV into the STM chamber and cooled to 5.0 K for STM measurements.

STM measurements

The microscopy and spectroscopy experiments are carried out in a UHV low-temperature STM system (CreaTec). STM topographic images are acquired in constant-current mode. The dI/dV and d^2I/dV^2 spectra are measured using the standard lock-in technique with a bias modulation of 8.0 mV (the stated value represents the amplitude of the modulation voltage, corresponding to root mean square value of ~5.7 mV) at 321.333 Hz. The d^2I/dV^2 spectra are analyzed by fitting them with a series of Gaussian peaks to determine the energy positions of the vibronic states. Multiple optimizations are conducted to achieve the best fitting outcomes. The STM tips are chemically etched tungsten, which are further calibrated spectroscopically against the Shockley surface states of cleaned Cu(111) or Au(111) surfaces before performing measurements on C_{60} islands/SnSe.

DFT calculations

First-principles DFT calculations are performed using the projector augmented wave method (*74*, *75*) with the Perdew-Burke-Ernzerhof (*76*) exchange correlation functional as implemented in the Vienna Ab Initio Simulation Package (*77*, *78*). The DFT-D3 correction (*79*) with zero-damping variant method is chosen for the vdW correction. A kinetic energy cutoff of 600 eV for the plane-wave basis set is used. The Brillouin zone is sampled using a uniform Γ-centered $1 \times 1 \times 1$ Monkhorst-pack *k*-mesh for structural relaxations and gamma-point vibration calculations. A 4×4 bilayer *Pnma* SnSe, with fixed bottom-layer atoms, is chosen as a substrate to describe the single-molecule adsorption sample (C_{60}-SnSe). A vacuum layer of ~18 Å is used to eliminate interactions between periodic structures. In structural relaxation, all atoms except the bottom layers SnSe are fully relaxed until the net force on every atom is less than 0.01 eV/Å. The gamma-point vibration frequencies of C_{60}-SnSe are calculated by finite differences method. The method of directly modifying the valence electron number of system is adopted to simulate charge doping.

The electronic charge density deformation potentials (V_{def}) is calculated following the strategy described in the reference (*69*). By using the generalized gradient approximation in the form of the Perdew-Burke-Ernzerhof functional, we solved the V_{def} using equation 3 in (*69*): $V_{def}(\mathbf{r}) = \sum_i \mathbf{Q}_i \cdot \nabla_i V_l[\rho(\mathbf{r}, \{\mathbf{R}\})]\Big|_{\{\mathbf{R}\}=\{\mathbf{R}^0\}} = \sum_i \frac{\partial V_l[\rho]}{\partial \rho}\mathbf{Q}_i \cdot \nabla_i \rho(\mathbf{r}, \{\mathbf{R}\})\Big|_{\{\mathbf{R}\}=\{\mathbf{R}^0\}}$ where $\{\mathbf{R}\}$ represents the set of ionic coordinates at the equilibrium position $\{\mathbf{R}^0\}$, $\mathbf{r}$ is defined as the vertical distance of a grid point away from the top Sn plane of the second-topmost SnSe substrate layer, $\mathbf{Q}_i$ represents the displacement field associated with the normal modes of the *i*th ion, and $V_l[\rho(\mathbf{r}, \{\mathbf{R}\})]$ included the Hartree and exchange correlation potential acting on the electrons. The either $H_g(\omega_1)$ or $H_g(\omega_2)$ mode is fivefold degenerate (fig. S11) (*34*). Combined with the fact that there are four typical adsorption structures [M_I, M_{II}, $M_{III(1)}$, and $M_{III(2)}$] observed for C_{60} on the SnSe surface, this results in 40 V_{def} curves in total. The number is doubled when further considering that the vibronic excitation process involves both ground and excited states, resulting in the 80 V_{def} curves (fig. S12) plotted along the surface normal direction as C_{60} is adsorbed on SnSe surface. To present these 80 curves in a high-readable manner, we integrated V_{def} and then average it for both the neutral and charged systems to obtain the deformation energy E_{def} and plotted them in Fig. 5B.

Supplementary Materials

This PDF file includes:

Supplementary Texts S1 to S4
Tables S1 and S2
Figs. S1 to S15

REFERENCES AND NOTES

1. A. Nitzan, M. A. Ratner, Electron transport in molecular wire junctions. *Science* **300**, 1384–1389 (2003).
2. M. Galperin, M. A. Ratner, A. Nitzan, A. Troisi, Nuclear coupling and polarization in molecular transport junctions: Beyond tunneling to function. *Science* **319**, 1056–1060 (2008).
3. R. Härtle, M. Butzin, O. Rubio-Pons, M. Thoss, Quantum interference and decoherence in single-molecule junctions: How vibrations induce electrical current. *Phys. Rev. Lett.* **107**, 046802 (2011).
4. X.-K. Chen, V. Coropceanu, J.-L. Brédas, Assessing the nature of the charge-transfer electronic states in organic solar cells. *Nat. Commun.* **9**, 5295 (2018).
5. F.-F. Kong, X.-J. Tian, Y. Zhang, Y.-J. Yu, S.-H. Jing, Y. Zhang, G.-J. Tian, Y. Luo, J.-L. Yang, Z.-C. Dong, J. G. Hou, Probing intramolecular vibronic coupling through vibronic-state imaging. *Nat. Commun.* **12**, 1280 (2021).
6. X. Bian, Z. Chen, J. K. Sowa, C. Evangeli, B. Limburg, J. L. Swett, J. Baugh, G. A. D. Briggs, H. L. Anderson, J. A. Mol, Charge-state dependent vibrational relaxation in a single-molecule junction. *Phys. Rev. Lett.* **129**, 207702 (2022).
7. F. Giustino, Electron-phonon interactions from first principles. *Rev. Mod. Phys.* **89**, 015003 (2017).
8. J. Nagamatsu, N. Nakagawa, T. Muranaka, Y. Zenitani, J. Akimitsu, Superconductivity at 39 K in magnesium diboride. *Nature* **410**, 63–64 (2001).
9. S. Gerber, S.-L. Yang, D. Zhu, H. Soifer, J. Sobota, S. Rebec, J. Lee, T. Jia, B. Moritz, C. Jia, Femtosecond electron-phonon lock-in by photoemission and x-ray free-electron laser. *Science* **357**, 71–75 (2017).
10. Y. He, M. Hashimoto, D. Song, S.-D. Chen, J. He, I. Vishik, B. Moritz, D.-H. Lee, N. Nagaosa, J. Zaanen, Rapid change of superconductivity and electron-phonon coupling through critical doping in Bi-2212. *Science* **362**, 62–65 (2018).
11. A. Lanzara, P. Bogdanov, X. Zhou, S. Kellar, D. Feng, E. Lu, T. Yoshida, H. Eisaki, A. Fujimori, K. Kishio, Evidence for ubiquitous strong electron-phonon coupling in high-temperature superconductors. *Nature* **412**, 510–514 (2001).
12. J. Bardeen, L. N. Cooper, J. R. Schrieffer, Theory of superconductivity. *Phys. Rev.* **108**, 1175–1204 (1957).
13. H. Park, J. Park, A. K. L. Lim, E. H. Anderson, A. P. Alivisatos, P. L. McEuen, Nanomechanical oscillations in a single-C_{60} transistor. *Nature* **407**, 57–60 (2000).
14. A. Pasupathy, J. Park, C. Chang, A. Soldatov, S. Lebedkin, R. Bialczak, J. Grose, L. Donev, J. Sethna, D. Ralph, Vibration-assisted electron tunneling in C_{140} transistors. *Nano Lett.* **5**, 203–207 (2005).
15. S. Ballmann, R. Härtle, P. B. Coto, M. Elbing, M. Mayor, M. R. Bryce, M. Thoss, H. B. Weber, Experimental evidence for quantum interference and vibrationally induced decoherence in single-molecule junctions. *Phys. Rev. Lett.* **109**, 056801 (2012).
16. J. Hihath, C. Bruot, N. Tao, Electron-phonon interactions in single octanedithiol molecular junctions. *ACS Nano* **4**, 3823–3830 (2010).
17. J. Franck, E. Dymond, Elementary processes of photochemical reactions. *Trans. Faraday Soc.* **21**, 536–542 (1926).
18. E. U. Condon, Nuclear motions associated with electron transitions in diatomic molecules. *Phys. Rev.* **32**, 858–872 (1928).
19. V. Gupta, *Principles and Applications of Quantum Chemistry* (Academic Press, 2016).
20. J. Repp, G. Meyer, S. Paavilainen, F. E. Olsson, M. Persson, Scanning tunneling spectroscopy of Cl vacancies in NaCl films: Strong electron-phonon coupling in double-barrier tunneling junctions. *Phys. Rev. Lett.* **95**, 225503 (2005).
21. N. Ogawa, G. Mikaelian, W. Ho, Spatial variations in submolecular vibronic spectroscopy on a thin insulating film. *Phys. Rev. Lett.* **98**, 166103 (2007).
22. G. Reecht, N. Krane, C. Lotze, L. Zhang, A. L. Briseno, K. J. Franke, Vibrational excitation mechanism in tunneling spectroscopy beyond the Franck-Condon model. *Phys. Rev. Lett.* **124**, 116804 (2020).
23. N. Pavliček, I. Swart, J. Niedenführ, G. Meyer, J. Repp, Symmetry dependence of vibration-assisted tunneling. *Phys. Rev. Lett.* **110**, 136101 (2013).
24. X. Qiu, G. V. Nazin, W. Ho, Vibronic states in single molecule electron transport. *Phys. Rev. Lett.* **92**, 206102 (2004).
25. N. A. Pradhan, N. Liu, W. Ho, Vibronic spectroscopy of single C_{60} molecules and monolayers with the STM. *J. Phys. Chem. B* **109**, 8513–8518 (2005).
26. H. Lee, J. Lee, W. Ho, Vibronic transitions in single metalloporphyrins. *ChemPhysChem* **6**, 971–975 (2005).
27. F. Matino, G. Schull, F. Köhler, S. Gabutti, M. Mayor, R. Berndt, Electronic decoupling of a cyclophane from a metal surface. *Proc. Natl. Acad. Sci. U.S.A.* **108**, 961–964 (2011).
28. J. Repp, P. Liljeroth, G. Meyer, Coherent electron-nuclear coupling in oligothiophene molecular wires. *Nat. Phys.* **6**, 975–979 (2010).
29. C. Li, C. Kaspar, P. Zhou, J.-C. Liu, O. Chahib, T. Glatzel, R. Häner, U. Aschauer, S. Decurtins, S.-X. Liu, Strong signature of electron-vibration coupling in molecules on Ag(111) triggered by tip-gated discharging. *Nat. Commun.* **14**, 5956 (2023).
30. N. Krane, C. Lotze, G. Reecht, L. Zhang, A. L. Briseno, K. J. Franke, High-resolution vibronic spectra of molecules on molybdenum disulfide allow for rotamer identification. *ACS Nano* **12**, 11698–11703 (2018).
31. F. Schwarz, Y. Wang, W. A. Hofer, R. Berndt, E. Runge, J. Kröger, Electronic and vibrational states of single tin-phthalocyanine molecules in double layers on Ag(111). *J. Phys. Chem. C* **119**, 15716–15722 (2015).
32. N. Sergueev, D. Roubtsov, H. Guo, Ab initio analysis of electron-phonon coupling in molecular devices. *Phys. Rev. Lett.* **95**, 146803 (2005).
33. H. Bi, C.-A. Palma, Y. Gong, K. Stallhofer, M. Nuber, C. Jing, F. Meggendorfer, S. Wen, C. Yam, R. Kienberger, Electron-phonon coupling in current-driven single-molecule junctions. *J. Am. Chem. Soc.* **142**, 3384–3391 (2020).
34. R. Heid, L. Pintschovius, J. Godard, Eigenvectors of internal vibrations of C_{60}: Theory and experiment. *Phys. Rev. B* **56**, 5925–5936 (1997).
35. N. Liu, N. Pradhan, W. Ho, Vibronic states in single molecules: C_{60} and C_{70} on ultrathin Al_2O_3 films. *J. Chem. Phys.* **120**, 11371–11375 (2004).
36. K. J. Franke, J. I. Pascual, Effects of electron–vibration coupling in transport through single molecules. *J. Phys. Condens. Matter* **24**, 394002 (2012).
37. T. Komeda, Chemical identification and manipulation of molecules by vibrational excitation via inelastic tunneling process with scanning tunneling microscopy. *Prog. Surf. Sci.* **78**, 41–85 (2005).
38. S. Trishin, C. Lotze, J. Richter, G. Reecht, N. Krane, P. Rietsch, S. Eigler, K. J. Franke, Variations of vibronic states in densely-packed structures of molecules with intramolecular dipoles. *Phys. Status Solidi* **221**, 2300105 (2024).
39. S.-U. Kim, A.-T. Duong, S. Cho, S. H. Rhim, J. Kim, A microscopic study investigating the structure of SnSe surfaces. *Surf. Sci.* **651**, 5–9 (2016).
40. G. Duvjir, T. Min, T. Thi Ly, T. Kim, A.-T. Duong, S. Cho, S. Rhim, J. Lee, J. Kim, Origin of p-type characteristics in a SnSe single crystal. *Appl. Phys. Lett.* **110**, 262106 (2017).
41. G. Mei, W. Tan, X. Cui, C. Wang, Q. Yuan, Y. Li, C. Lou, X. Hou, M. Zhao, Y. Liu, Room-temperature ferromagnetism in Fe-doped SnSe bulk single crystalline semiconductor. *Mater. Today Phys.* **38**, 101251 (2023).
42. T. Hashizume, K. Motai, X. Wang, H. Shinohara, Y. Saito, Y. Maruyama, K. Ohno, Y. Kawazoe, Y. Nishina, H. Pickering, Intramolecular structures of C_{60} molecules adsorbed on the Cu(111)-(1×1) surface. *Phys. Rev. Lett.* **71**, 2959–2962 (1993).
43. M. Grobis, X. Lu, M. Crommie, Local electronic properties of a molecular monolayer: C_{60} on Ag(001). *Phys. Rev. B* **66**, 161408 (2002).
44. X. Lu, M. Grobis, K. Khoo, S. G. Louie, M. Crommie, Charge transfer and screening in individual C_{60} molecules on metal substrates: A scanning tunneling spectroscopy and theoretical study. *Phys. Rev. B* **70**, 115418 (2004).

45. J. A. Larsson, S. D. Elliott, J. C. Greer, J. Repp, G. Meyer, R. Allenspach, Orientation of individual C_{60} molecules adsorbed on Cu(111): Low-temperature scanning tunneling microscopy and density functional calculations. *Phys. Rev. B* **77**, 115434 (2008).
46. H. Shin, A. Schwarze, R. Diehl, K. Pussi, A. Colombier, É. Gaudry, J. Ledieu, G. McGuirk, L. S. Loli, V. Fournée, Structure and dynamics of C_{60} molecules on Au(111). *Phys. Rev. B* **89**, 245428 (2014).
47. T. Frederiksen, K. J. Franke, A. Arnau, G. Schulze, J. I. Pascual, N. Lorente, Dynamic Jahn-Teller effect in electronic transport through single C_{60} molecules. *Phys. Rev. B* **78**, 233401 (2008).
48. N. Manini, E. Tosatti, A. Auerbach, Electron-vibron interactions in charged fullerenes. II. Pair energies and spectra. *Phys. Rev. B* **49**, 13008–13016 (1994).
49. J. Zhou, R. Xu, X. Yu, F. Cheng, W. Zhao, X. Du, S. Wang, Q. Zhang, X. Gu, S. He, Evidence for band renormalizations in strong-coupling superconducting alkali-fulleride films. *Phys. Rev. Lett.* **130**, 216004 (2023).
50. N. Manini, P. Gattari, E. Tosatti, Jahn-Teller spectral fingerprint in molecular photoemission: C_{60}. *Phys. Rev. Lett.* **91**, 196402 (2003).
51. O. Gunnarsson, H. Handschuh, P. S. Bechthold, B. Kessler, G. Ganteför, W. Eberhardt, Photoemission spectra of C_{60}^-: Electron-phonon coupling, Jahn-Teller effect, and superconductivity in the fullerides. *Phys. Rev. Lett.* **74**, 1875–1878 (1995).
52. O. Gunnarsson, Superconductivity in fullerides. *Rev. Mod. Phys.* **69**, 575–606 (1997).
53. M. Wolf, E. Knoesel, T. Hertel, Ultrafast dynamics of electrons in image-potential states on clean and Xe-covered Cu(111). *Phys. Rev. B* **54**, R5295–R5298 (1996).
54. A. Damm, K. Schubert, J. Güdde, U. Höfer, Observation of the transition from image-potential states to resonances on argon-covered Cu(111) and Ag(111) by time-resolved two-photon photoemission. *Phys. Rev. B* **80**, 205425 (2009).
55. P. Echenique, J. Pendry, The existence and detection of Rydberg states at surfaces. *J. Phys. C Solid State Phys.* **11**, 2065–2075 (1978).
56. G. Herzberg, *Electronic Spectra and Electronic Structure of Polyatomic Molecules* (Van Nostrand, 1966).
57. G. D. Mahan, *Many–Particle Physics* (Springer Science & Business Media, 2000).
58. P. Zhou, K. A. Wang, Y. Wang, P. C. Eklund, M. S. Dresselhaus, G. Dresselhaus, R. A. Jishi, Raman scattering in C_{60} and alkali-metal-saturated C_{60}. *Phys. Rev. B* **46**, 2595–2605 (1992).
59. B. J. LeRoy, S. Lemay, J. Kong, C. Dekker, Electrical generation and absorption of phonons in carbon nanotubes. *Nature* **432**, 371–374 (2004).
60. S. Sapmaz, P. Jarillo-Herrero, Y. M. Blanter, C. Dekker, H. Van Der Zant, Tunneling in suspended carbon nanotubes assisted by longitudinal phonons. *Phys. Rev. Lett.* **96**, 026801 (2006).
61. R. Leturcq, C. Stampfer, K. Inderbitzin, L. Durrer, C. Hierold, E. Mariani, M. G. Schultz, F. Von Oppen, K. Ensslin, Franck–Condon blockade in suspended carbon nanotube quantum dots. *Nat. Phys.* **5**, 327–331 (2009).
62. V. Coropceanu, J. Cornil, D. A. da Silva Filho, Y. Olivier, R. Silbey, J.-L. Brédas, Charge transport in organic semiconductors. *Chem. Rev.* **107**, 926–952 (2007).
63. R. M. Metzger, *Unimolecular and Supramolecular Electronics I: Chemistry and Physics Meet at Metal-Molecule Interfaces* (Springer Science & Business Media, 2012), vol. 312.
64. S. Meierott, N. Néel, J. Kröger, Line shapes in inelastic electron tunneling spectroscopy of single-molecule junctions. *Phys. Rev. B* **96**, 205437 (2017).
65. B. C. Stipe, M. A. Rezaei, W. Ho, Single-molecule vibrational spectroscopy and microscopy. *Science* **280**, 1732–1735 (1998).
66. W. Ho, Single-molecule chemistry. *J. Chem. Phys.* **117**, 11033–11061 (2002).
67. J. H. Frederick, Y. Fujiwara, J. H. Penn, K. Yoshihara, H. Petek, Models for stilbene photoisomerization: Experimental and theoretical studies of the excited-state dynamics of 1,2-diphenylcycloalkenes. *J. Phys. Chem.* **95**, 2845–2858 (1991).
68. A. Garcia-Lekue, D. Sanchez-Portal, A. Arnau, T. Frederiksen, Simulation of inelastic electron tunneling spectroscopy of single molecules with functionalized tips. *Phys. Rev. B* **83**, 155417 (2011).
69. N. Breda, R. Broglia, G. Colò, H. Roman, F. Alasia, G. Onida, V. Ponomarev, E. Vigezzi, Electron–phonon coupling in charged buckminsterfullerene. *Chem. Phys. Lett.* **286**, 350–354 (1998).
70. D. Li, Z. Peng, L. Deng, Y. Shen, Y. Zhou, Theoretical studies on molecular structure and vibrational spectra of copper phthalocyanine. *Vib. Spectrosc.* **39**, 191–199 (2005).
71. T. V. Basova, V. G. Kiselev, B. E. Schuster, H. Peisert, T. Chasse, Experimental and theoretical investigation of vibrational spectra of copper phthalocyanine: Polarized single-crystal Raman spectra, isotope effect and DFT calculations. *J. Raman Spectrosc.* **40**, 2080–2087 (2009).
72. C. Jiao, K. Huang, H. Guo, X. Cui, Q. Yuan, C. Lou, G. Mei, C. Wu, N. Xu, L. Cao, Resonant four-photon photoemission from $SnSe_2$ (001). *Front. Phys.* **19**, 33207 (2024).
73. B. Li, J. Zhao, K. Onda, K. D. Jordan, J. Yang, H. Petek, Ultrafast interfacial proton-coupled electron transfer. *Science* **311**, 1436–1440 (2006).
74. G. Kresse, D. Joubert, From ultrasoft pseudopotentials to the projector augmented-wave method. *Phys. Rev. B* **59**, 1758–1775 (1999).
75. P. E. Blöchl, Projector augmented-wave method. *Phys. Rev. B* **50**, 17953–17979 (1994).
76. J. P. Perdew, K. Burke, M. Ernzerhof, Perdew, burke, and ernzerhof reply. *Phys. Rev. Lett.* **80**, 891 (1998).
77. G. Kresse, J. Furthmüller, Efficient iterative schemes for ab initio total-energy calculations using a plane-wave basis set. *Phys. Rev. B* **54**, 11169–11186 (1996).
78. G. Kresse, J. Furthmüller, Efficiency of ab-initio total energy calculations for metals and semiconductors using a plane-wave basis set. *Comput. Mater. Sci.* **6**, 15–50 (1996).
79. S. Grimme, J. Antony, S. Ehrlich, H. Krieg, A consistent and accurate ab initio parametrization of density functional dispersion correction (DFT-D) for the 94 elements H-Pu. *J. Chem. Phys.* **132**, 154104 (2010).

Acknowledgments: We acknowledge discussions with C. Lin, L. Mao, and R. Yu. **Funding:** This work was supported by National Key R&D Program of China 2018YFA0305802 and 2017YFA0303500; Strategic Priority Research Program of Chinese Academy of Sciences XD30000000; National Natural Science Foundation of China 11774267, 61674171, and 11974422; Fundamental Research Funds for the Central Universities and the Research Funds of Renmin University of China 22XNKJ30; Luo Jia Visiting Chair Professorship at Wuhan University; NSF CHE-2102601. All calculations for this study were performed at the Physics Lab of High-Performance Computing (PLHPC) and the Public Computing Cloud (PCC) of Renmin University of China. **Author contributions:** Project administration: W.J. and M.F. Funding acquisition: W.J. and M.F. Conceptualization: L.C., D.N., H.P., W.J., and M.F. Methodology: C.L., Y.G., X.C., X.Z., L.C., D.N., W.J., and M.F. Formal analysis: Y.G., X.Z., and W.J. Software: Y.G. and X.Z. Investigation: C.L., Y.G., X.C., Y.L., X.Z., Q.Y., G.M., C.J., K.H., and X.H. Visualization: C.L., Y.G., X.C., X.Z., and H.P. Supervision: L.C., H.P., W.J., and M.F. Data curation: H.P. Resources: G.M., W.J., H.P., and M.F. Writing—original draft: C.L. and M.F. Writing—review and editing: C.L., Y.G., X.C., L.C., W.J., H.P., and M.F. Validation: W.J., H.P., and M.F. **Competing interests:** The authors declare that they have no competing interests. **Data and materials availability:** All data needed to evaluate the conclusions in the paper are present in the paper and/or the Supplementary Materials.

Submitted 29 January 2024
Accepted 18 September 2024
Published 23 October 2024
10.1126/sciadv.ado3470